Binary pseudo random array standards for calibration of 3D optical surface profilers used for metrology with significantly curved x-ray optics

K. Munechika[a], K. Yamada[a], S. Rochester[b], H. Barnard[d], W. Chao[c], I. Lacey[d], C. Pina-Hernandez[a], P. Z. Takacs[e], and V. V. Yashchuk[d]

[a]HighRI Optics, Inc., 5401 Broadway Terr, St. 304, Oakland, California 94618, USA; [e]Rochester Scientific, LLC, 2041 Tapscott Avenue, El Cerrito, CA 94530, USA; [c]Center for X-ray Optics, Lawrence Berkeley National Laboratory, Berkeley, California, 94720, USA; [d]Advanced Light Source, Lawrence Berkeley National Laboratory, Berkeley, California 94720, USA; [e]Surface Metrology Solutions LLC, 19 S 1st St, Unit B901, Minneapolis, MN 55401 USA

ABSTRACT

High-accuracy metrology is vitally important in manufacturing ultra-high-quality free-form mirrors designed to manipulate X-ray light with nanometer-scale wavelengths. The current capabilities and possibility for improvements in X-ray mirror manufacturing are limited by inherent imperfections of the integrated metrology tools. In the case of Fizeau interferometry, metrology tools are currently calibrated with super-polished flat test-standard/reference mirrors. This is acceptable for measuring slightly curved X-ray optics. However, for even moderately curved aspherical X-ray mirrors the flat-reference calibration is not sufficiently accurate and stitching Fizeau interferometer-based surface metrology is used to mitigate the problem. But still, the retrace and aberration errors, as well as the limited spatial resolution, described with the instrument transfer function (ITF), can be transferred into the optical surface topography of X-ray mirrors obtained in stitching metrology. For ITF calibration, we have developed an original technique, based on test standards structured as two-dimensional (2D) highly-randomized (HR) binary pseudo-random arrays (BPRAs). The technique employs the unique properties of the HR BPRA patterns in the spatial frequency domain., i.e. the inherent 2D power spectral density of the HR BPRA pattern has a deterministic white-noise-like character that allows direct determination of the ITF with uniform sensitivity over the entire spatial frequency range and field-of-view of an instrument. Here, we explore technological, metrological, and analytical aspects essential for calibration of the retrace and aberration errors of Fizeau interferometers using different types of tilted test samples, including a super-polished reference mirror for the re-trace calibration and the uniformly redundant array (URA) BPRA standards for the geometrical distortion (aberration) calibration. While the first method was previously demonstrated by researchers at DIAMOND Light Source, a method based on the URA BPRA is described and demonstrated here for the first time. We outline the design and fabrication process used in fabrication of URA BPRA test standards, and present the results of application of the URA BPRA standards demonstrating the high efficacy of our approach to geometrical distortion calibration of Fizeau interferometers. We also discuss the possible sources of unexpected peculiarities of the systematic errors, including an astigmatic character of the retrace error, observed with Fizeau interferometers at the Advanced Light Source X-Ray Optics Laboratory.

Keywords: Fizeau interferometer, retrace errors, geometrical distortion, calibration, binary pseudo-random, test standard, instrument transfer function, stitching surface metrology

1. INTRODUCTION

Optical manufacturing is a multi-billion-dollar industry that is an indispensable part of modern technology and science. The performance of any optical manufacturing process directly depends on the ability of its integrated optical surface metrology method to provide trustworthy feedback. High-accuracy metrology is vitally important in manufacturing ultra-high-quality aspheric and free-form mirrors, such as paraboloids, ellipsoids, hyperbolas, diaboloids (see, for example, Refs. [1-6] and references therein), designed to manipulate X-ray light with nanometer-scale wavelengths.

*Corresponding author: km@highrioptics.com; phone 1-(800) 470-7902; https://highrioptics.com/

Due to the short wavelengths, requirements for the surface figure and finish of X-ray mirrors are three orders of magnitude more stringent than for visible-light optics. Correspondingly, the metrology integrated into X-ray mirror manufacturing must ensure the accuracy of optical surface fabrication at the sub-nanometer level. Due to the grazing-incidence application of X-ray mirrors, high accuracy metrology must be capable of characterization over strongly asymmetrical clear apertures with the tangential length of up to a meter or even more. Availability of such free-form X-ray mirrors on the market will directly advance the fundamental and applied research performed at the DOE X-ray source facilities.

The current capabilities and possibility for improvements in X-ray mirror manufacturing are limited by inherent imperfections in the integrated metrology tools. Developing new higher-accuracy metrology instruments to replace the currently integrated tools would be a slow, expensive, and uncertain process. A much more attractive approach is to improve the existing tools by developing calibration techniques to thoroughly characterize them and then to process the data to remove the effects of their imperfections.

Metrology tools are currently calibrated with super-polished flat test-standard/reference mirrors. This is acceptable for fabrication of slightly curved X-ray optics. However, for even moderately curved aspherical X-ray mirrors the flat-reference calibration is not sufficiently accurate. Thus, the aberration errors of the stitching metrology used in the Elastic Emission Machining (EEM) deterministic nano-fabrication process [7-9], which can depend on the surface curvature, are often transferred into the optical surface topography of X-ray mirrors where they result in quasi-periodic errors in the surface height and slope [10].

For highly curved aspherical optics specified with nanometer or smaller height tolerances, obtaining surface metrology data with adequate accuracy is an extremely challenging task. The limited accuracy of the available metrology has led to an absence in the market of such X-ray mirrors required for modern applications. It is the deficiencies in the metrology, rather than in the fabrication technologies (such as the EEM and Electron and Ion Beam Figuring, EBF and IBF, techniques) that primarily limits the optical quality. Therefore, advanced integrated metrology is key to the improvement of optical manufacturing.

For decades, plane wavefront Fizeau interferometry (PWFI) has been one of the major metrology techniques for surface characterization of x-ray optics in the low and middle spatial frequency range (see, for example, Refs. [11-13] and references therein). However, the application of the technique for metrology with large-radius tangentially-curved optics is known to be associated with a number of systematic errors. The error that arises because of the difference between the optical paths of the reference beam and the light reflected off the surface under test (SUT) is the well-known retrace error [13-15]. A less-investigated source of error is geometrical distortion (GD) (see the discussion in Refs. [6,7]). Other errors in PWFI arise from limited spatial resolution, leading to systematic effects in the spatial frequency domain that are usually characterized by the instrument transfer function (ITF) [18-20]. Measurement errors of the same nature appear also in the measurements of a misaligned plane SUT.

For ITF calibration, we have developed an original technique [21-25], based on test standards structured as two-dimensional (2D) highly-randomized (HR) binary pseudo-random arrays (BPRAs). The technique employs the unique properties of the HR BPRA patterns in the spatial frequency domain, i.e. the inherent 2D power spectral density of the HR BPRA pattern that has a deterministic white-noise-like character that allows direct determination of the ITF with uniform sensitivity over the entire spatial frequency range and field-of-view of an instrument. The results and discussion of the ITF calibration of Fizeau interferometers available at the Advanced Light Source (ALS) X-Ray Optics Laboratory [26] can be found in Ref. [27].

Here, we explore technological, metrological, and analytical aspects essential for calibration of the retrace and aberration errors of Fizeau interferometers using different type of tilted test samples, including a super-polished reference mirror for the re-trace calibration and the uniformly redundant array (URA) BPRA standards for the geometrical distortion (aberration) calibration. While the first method was previously demonstrated by researchers at DIAMOND Light Source [15] (see also Sec. 2), a method based on the URA BPRA is described and demonstrated here for the first time. We outline the design and fabrication process used for development of URA BPRA test standards, and present the results of application of the URA BPRA standards and an original data deconvolution software demonstrating the high efficacy of our approach to geometrical distortion calibration of Fizeau interferometers. We also discuss the possible sources of unexpected peculiarities of the systematic errors, including an astigmatic character of the retrace error, observed with Fizeau interferometers at the ALS XROL.

2. RETRACE ERROR OF THE ALS XROL FIZEAU INTERFEROMETERS IN MEASUREMENTS WITH A TILTED PLANE REFERENCE MIRROR

It has been long recognized that high-accuracy surface shape measurements using conventional laser Fizeau interferometers are affected by a specific systematic error, knowns as retrace (propagation) error [13-15,28-30]. The retrace error appears due to the aberrations in the optical system of the interferometer and the surface under test (SUT) related to the optical path difference (OPD) of the rays from the SUT and those from the interferometer's reference surface. In the case of the conventional interferometric optical testing of plane and spherical mirrors in a single-fringe-interference arrangement (that is *perfectly aligned*) with the plane and spherical transmission references, the retrace error may be negligible. However, when the SUT is aspherical, as necessary, for example, for focusing x-ray mirrors, the difference between the SUT and reference optical paths can strongly perturb the measured interference fringe pattern, leading to non-negligible retrace error that can be as large as 100 nm peak-to-valley (PV).

Figure 1 illustrates the importance of the retrace error even in the case of measurements with a slightly curved cylindrical x-ray optic with a radius of curvature (ROC) of 120 meters using the ALS XROL 6-in aperture Fizeau interferometer Verifire™. In Fig.1, the retrace error is seen as a residual (after detrending of the best-fit cylindrical surface) height variation of ~120 nm PV that is unchanged when the SUT is measured in the direct (Fig. 1a) and in the end-to-end flipped (Fig. 1b) orientations. The fact that this observed variation is spurious is confirmed by measurements of the same optic with a surface slope profiler OSMS [31] available at the ALS XROL that show a residual surface error on the level of only a few nanometers (Fig. 1b).

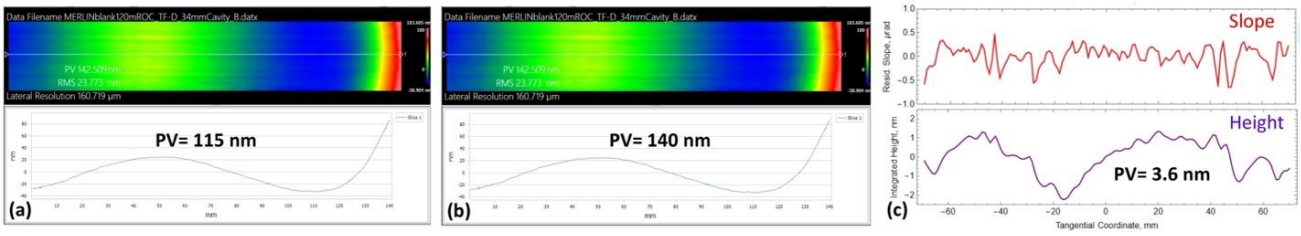

Figure 1: Illustration of the retrace error contribution to the PWFI measurements with a cylindrical x-ray optic with ROC of 120 meters. The residual (after detrending of the best-fit cylindrical surface) height variations as measured with the SUT (a) in the direct and (b) in the end-to-end flipped orientation; the corresponding PV variations are 115 nm and 140 nm, respectively. (c) The results of measurements of the same optic with the ALS XROL OSMS slope profiler OSMS [31] in the slope (the top plot) and in the height (the bottom plot) domains; the surface error measured with the OSMS is 3.6 nm (PV).

The retrace error in a particular measurement depends on the shape, tilt, and focus (lateral position) of the SUT (see, for example, Refs. [15,32] and references therein). Below in this section, we present and discuss the results of the retrace error PWFI measurement with a tilted plane reference mirror.

2.1. Experimental arrangement

Figure 2 depicts the experimental arrangement of the PWFI measurement with a tilted plane reference mirror performed with the ALS XROL Fizeau interferometers Verifire™ (Fig. 2a) and DynaFiz™ (Fig. 2b)

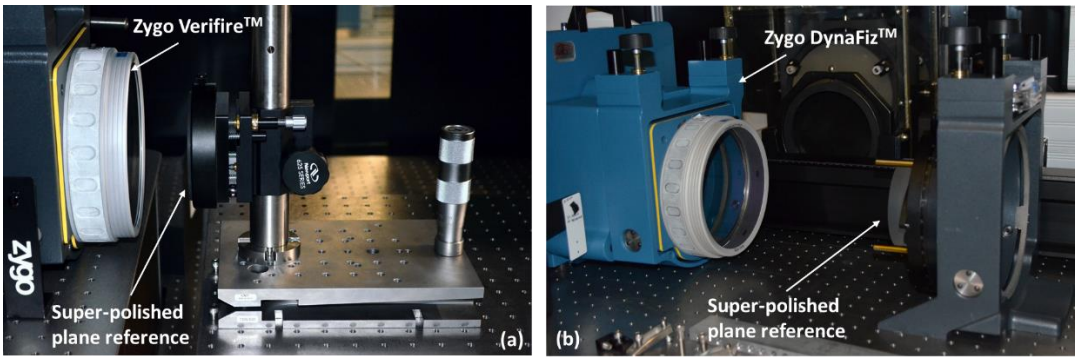

Figure 2: Experimental setup of the ALS XROL 6-in aperture Fizeau interferometers (a) Verifire™ and (b) Zygo DynaFiz™, equipped with flat transmission references and used for measurements with a super-polished 4-in diameter plane reference mirror at different tilts.

2.2. An astigmatic character of the retrace error in PWFI measurements with tilted plane mirror

Figure 3 presents a screenshot of the Zygo Mx™ software window showing the result of the Verifire™ measurement with the super-polished 4-in diameter plane reference mirror in a single-fringe-interference arrangement. The surface topography observed in this case can be thought of as a baseline shape due to the inherent shape variation of the reference mirror (specified for the surface figure error to be below ~ λ/40, λ ≈ 632.8 nm) and the shape error due to the limited quality of the tool's plane transmission reference (specified to be below ~ λ /50).

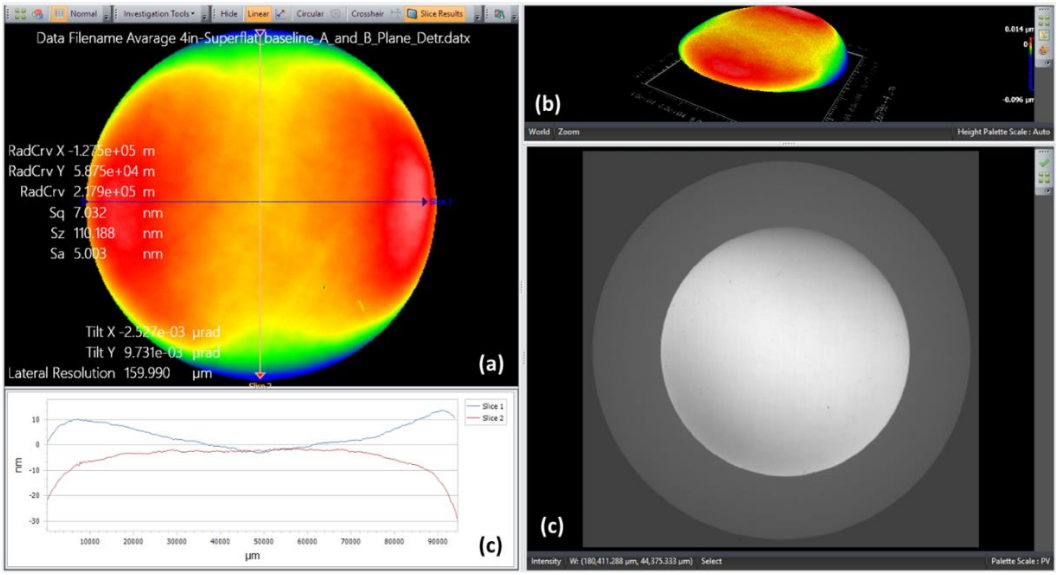

Figure 3: Screenshot of the instrument's Zygo Mx™ software window showing the result of the Verifire™ measurement with the perfectly aligned 4-in diameter plane reference mirror: (a) two-dimensional and (b) three-dimensional images of the measured topography, (c) the measured height variations along the horizontal (the blue line) and vertical (the red line) cross-sections, and (d) the single-fringe-interference pattern corresponding to the experimental arrangement with the perfectly aligned (no tilt) SUT.

The results of measurements in the same arrangement as in Fig. 3 but with the plane reference mirror tilted in the vertical direction (around the horizontal axis) by 99 µrad, 201 µrad, and 506 µrad are shown in Figs. 4, 5, and 6, respectively.

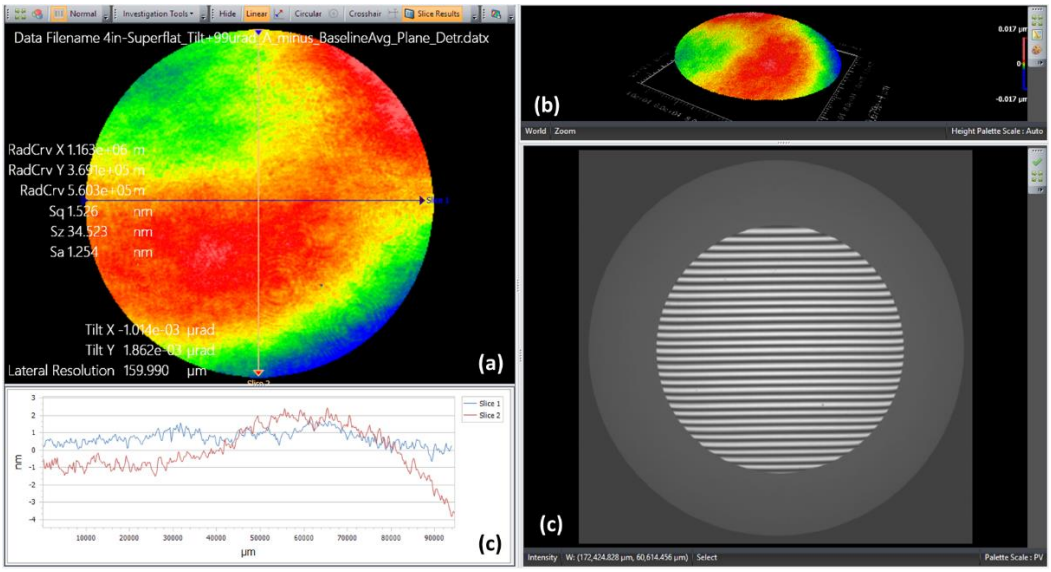

Figure 4: Screenshot of the instrument's Zygo Mx™ software window showing the result of the Verifire™ measurement analogous to the one in Fig. 3, but obtained with the plane reference mirror vertically tilted by 99 µrad. The baseline measurement in Fig. 3 is subtracted from the measurement with tilted plane reference shown here.

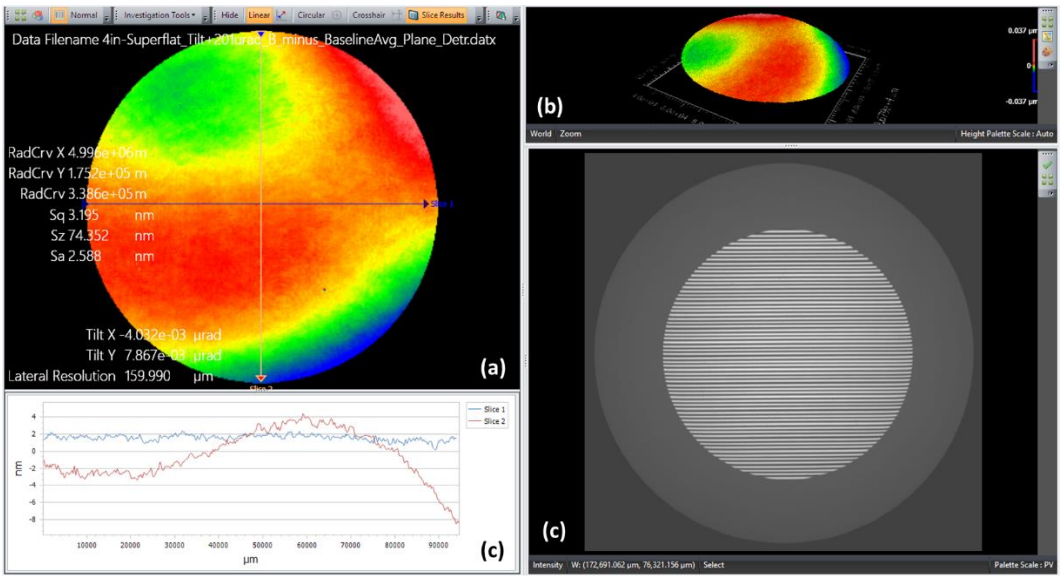

Figure 5: Screenshot of the instrument's Zygo Mx™ software window showing the result of the Verifire™ measurement analogous to the one in Fig. 3, but obtained with the plane reference mirror vertically tilted by 201 µrad. The baseline measurement in Fig. 3 is subtracted from the measurement with tilted plane reference shown here.

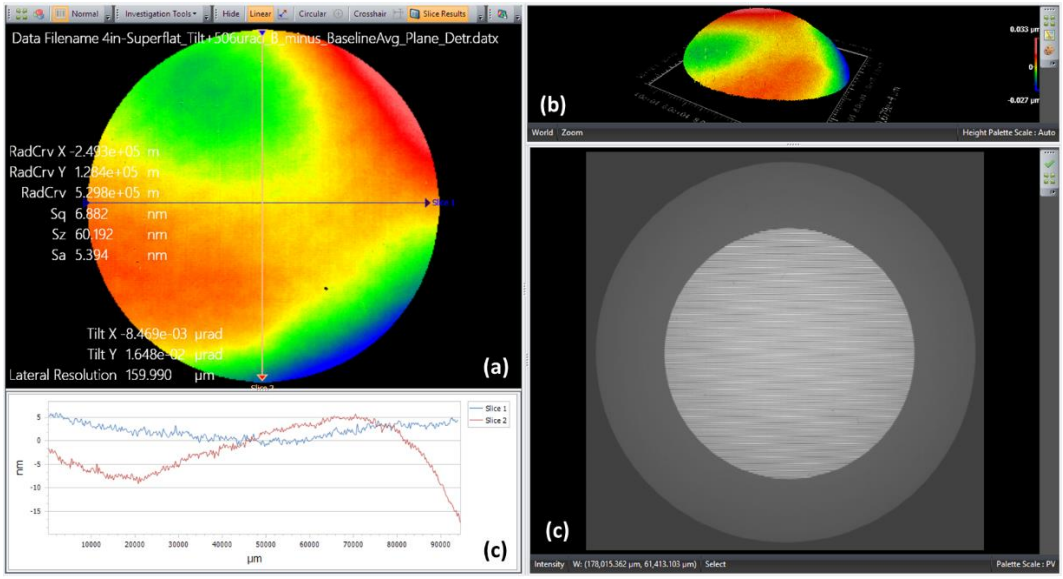

Figure 6: Screenshot of the instrument's Zygo Mx™ software window showing the result of the Verifire™ measurement analogous to the one in Fig. 3, but obtained with the plane reference mirror vertically tilted by 506 µrad. The baseline measurement in Fig. 3 is subtracted from the measurement with tilted plane reference shown here.

The overall shape of the retrace error topography depicted in Figs. 4-6 does not depend on the value of the tilt angle, whereas the magnitude of the error scales almost linearly when the tilt angle is varying between ~ 100 µrad and 500 µrad, applied in these measurements. A removable observation from the measurements is the strong astigmatic shape of the retrace error topography that does not correspond to a symmetrical (with respect to the vertical axis) shape expected for measurement with a vertical tilted plane SUT.

Note that similar measurements performed with the ALS XROL Zygo DynaFiz™ interferometer are resulted in basically a similar astigmatic character of the retrace angle. However, the overall magnitude of the error is a factor of ~ 2 smaller. This is probably due to a specificity of the tool's design optimized for dynamic measurements in the presence of vibrations or air turbulence. Unfortunately, due to its proprietary nature, information about how this is accomplished is very limited and not well-documented [33].

2.3. An astigmatic character of the retrace error in PWFI measurements with tilted plane mirror

To investigate and understand the origin of the astigmatic shape of the retrace error measured with the ALS XROL Fizeau interferometers (Sec. 2.2), we develop an interferometer model using Zemax OpticStudio™ with an ideal transmission flat and use it to simulate retrace errors from a tilted plane SUT. The problem, however, is that we have no information about the proprietary design parameters of the internal optics of the commercial interferometers in use. We need to make a best guess as to what the internal collimator lens design might be. To this end, we use as a starting point the results in a paper by Peng, et al. [34]. The Fizeau system in Ref. [34] is designed to investigate error tolerances in a transmission sphere design. Therefore, we have modified the design to investigate errors produced by a system with a transmission flat by starting with a simple model of a collimator with a test flat element and a plane mirror reflecting the wavefront back through the system. This simple model is enhanced by adding an imaging module that projects the SUT onto the detector plane with minimum added aberration – Fig. 7.

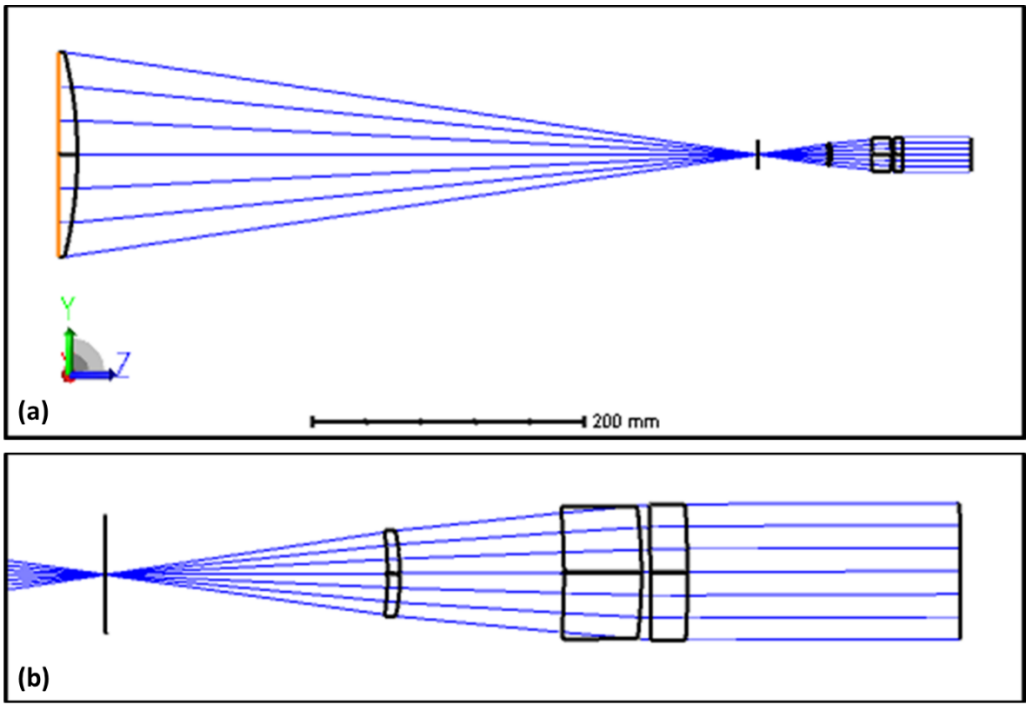

Figure 7: Fizeau interferometer design incorporating imaging optics to focus the SUT onto the detector: (a) the return beam arm diagram and (b) configuration of the imaging elements beyond the aperture stop at the focus of the collimator.

In Fig. 7a, only the return rays are shown, coming from the plano REF surface of the collimating lens on the left. In this design, the collimating lens is simplified, using only a single plano-convex element with an aspheric surface on the convex surface. In actual practice, there is a beam splitter placed between the collimating lens and the focal point to separate the outgoing and incoming beams. The closeup of the imaging optics in Fig. 7b shows how the rays are relayed from the aperture stop at the focal point on the left, to the detector plane on the right. The system is designed to image the 150 mm × 150 mm SUT onto a 25 mm × 25 mm camera surface.

Figure 8 shows the quality of the reference (REF) wavefront on the camera. The peak-to-valley (PV) wavefront error is 0.0084 waves and the root-mean-square (RMS) is 0.0025 waves. It is essentially diffraction limited.

With this system design, tilting the SUT clearly shows the effect of retrace errors on the measured wavefront. Figure 9 shows the expected interferogram (Fig. 9a) and (Fig. 9b) wavefront for a plano SUT tilted by 10 μrad about the horizontal axis. This tilt produces 4.8 fringes in the interferogram and 0.126 waves PV of wavefront error.

After removing the tilt component and REF wavefront (Fig. 9c), the residual becomes 0.0411 waves PV, or 0.0078 waves RMS. This shows how retrace error distorts a plane surface into one that contains mainly coma. For larger SUT tilt values, the RMS coma error scales linearly with tilt angle.

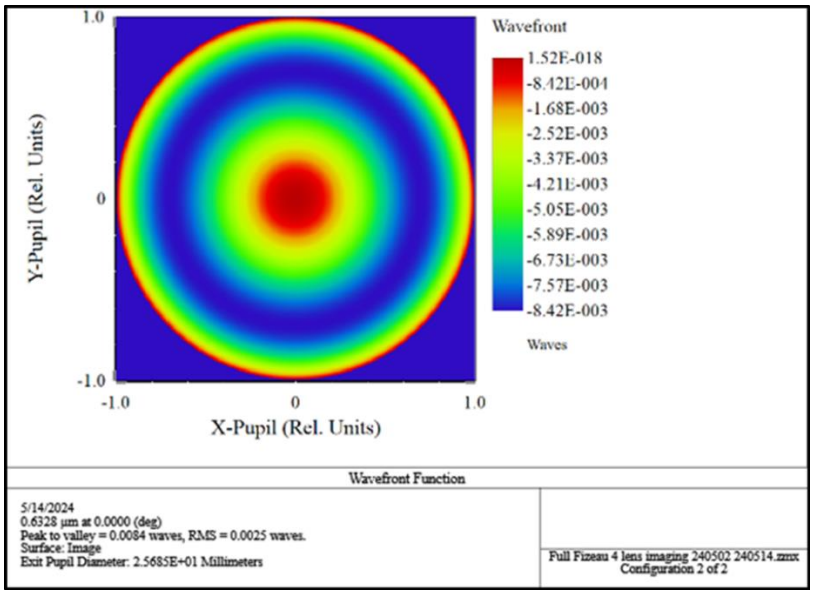

Figure 8: Reference wavefront for the interferometer design in Fig. 7 evaluated with the perfectly aligned plane SUT.

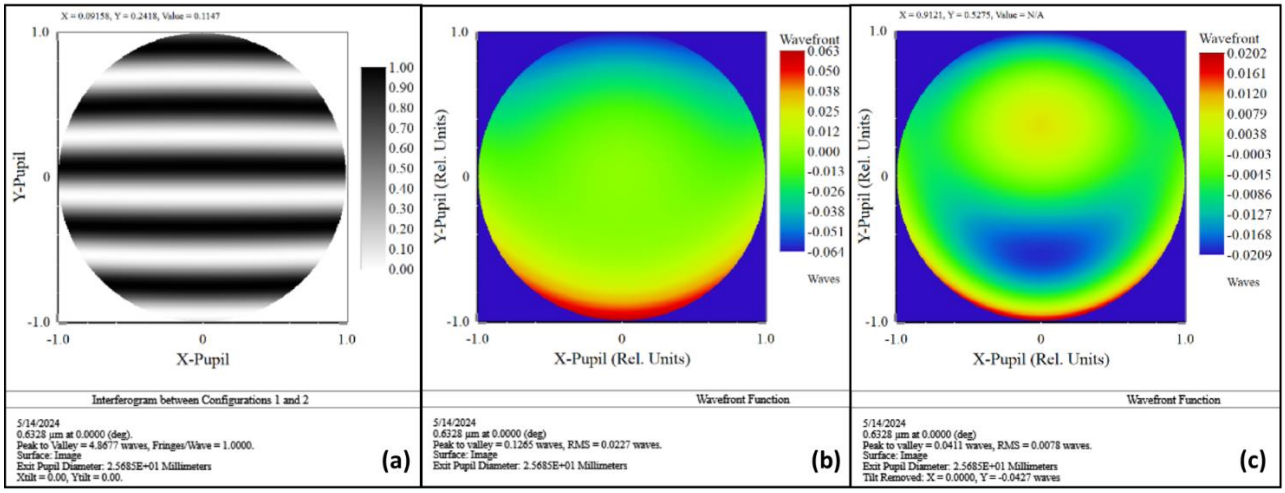

Figure 9: The interferogram (a) and (b) wavefront error simulated with the plane SUT tilted by 10 µrad in the vertical direction; (c) the residual wavefront error after removing the tilt term and REF wavefront. The residual error is mainly coma and scales linearly with tilt angle.

Note that as expected, the simulation in Fig. 9 with an ideally aligned optical design of the interferometer and vertically tilted SUT results in the retrace error that is symmetrical with respect to the vertical axis.

However, as we have shown in Sec. 2.2, an actual measurements with a Verifire™ interferometer on a high-quality flat mirror tilted about the horizontal axis (Figs. 4-6) depict the residual error with a more complicated structure than in the simulation shown in Fig. 9. The measured retrace error is not aligned with the tilt direction, having an astigmatic shape.

The astigmatism signature of the retrace error can be thought of as an indication of a possible lens element decenter. In order to check this hypotesis, we performed the raytrace simulation outlined above with an interferometer model with a 5-element collimating lens with the middle lens element (L3) decentered by 50 µm in both the x- and y-directions – Fig. 10. In Fig. 10, the baseline wavefront is not subtracted from the simulation. In any case, it shows how the decenter in X and Y introduces a small amount of astigmatism in the retrace error with the shape, similar to the measured wavefront in Figs. 4-6. The RMS wavefront error in Fig.10 is 18.8 nm. More work is needed to understand the nature of the possible lens decenter error in the Verifire™ instrument.

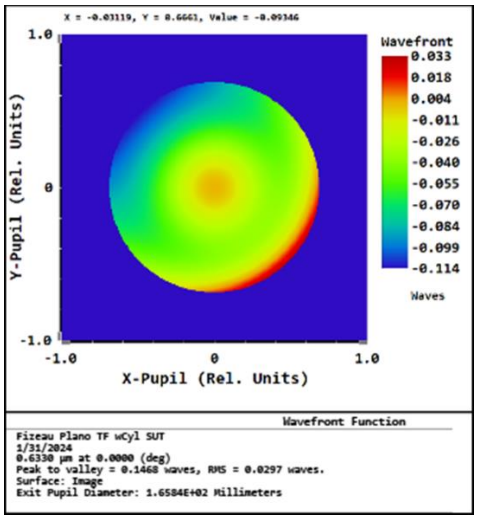

Figure 10: Baseline wavefront of the Fizeau model with the middle (L3) lens element decentered by 50 µm in the X and Y directions. The generated wavefront error is similar to the observed astigmatic retrace error shown in Fig. 4-6.

Note that OpticStudio does not use phase shifting of interference fringes to compute wavefront error. It does not average the intensity within a detector pixel, which reduces contrast and would limit the usable fringe density and SUT tilt angle. It only uses the optical path length along a ray that has infinitesimal lateral dimensions, so there is no limit on fringe density in these wavefront simulations. For large tilt angles, we expect deviations between measurement and simulation, but small tilt angle simulations should reproduce measurement errors closely.

3. NOVEL APPROACH TO ENABLE GEOMETRICAL DISTORTION CALIBRATION OF FIZEAU INTERFEROMETERS

3.1. Design considerations for the test artifact for geometrical distortion calibration

In our previous work on calibration of the geometrical distortion (GD) of interferometric microscopes [35,36], we have developed a number of test samples designed according to the checkerboard (CB) and uniformly redundant array patterns. We have also developed a prototype software optimized for processing the GD calibration data and the corresponding correction of the surface topography measurements with interferometric microscopes.

Based on the success of this preliminary work and because of the availability of a very sophisticated code specially developed for processing of the CB data, we first chose to test the checkerboard test artifacts for GD calibration of a Fizeau interferometer. A fabricated CB sample with an elementary feature size of 300 µm was measured with the ALS XROL 6-in aperture Fizeau interferometer Zygo™ DynaFiz with the spatial resolution adjusted to 80 µm (see Fig. 11).

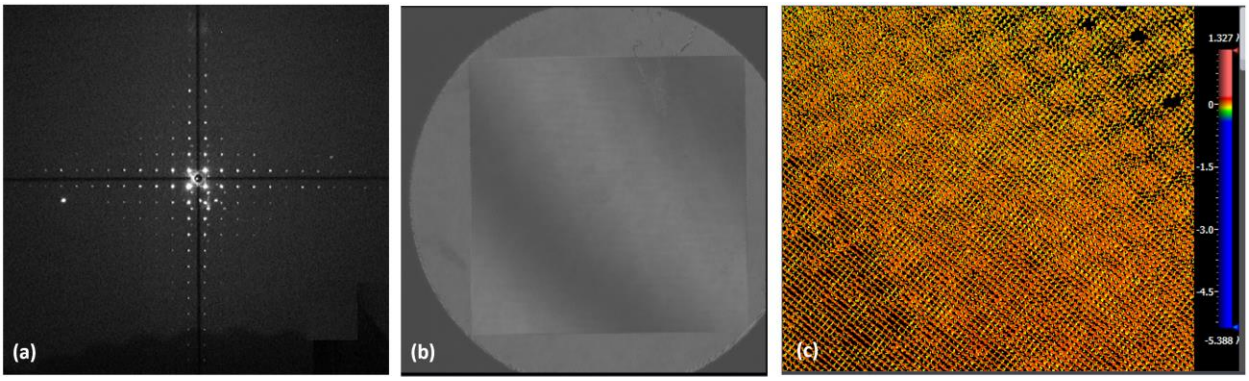

Figure 11: The checkerboard sample with 300 um elementary size as measured with the ALS XROL Zygo™ DynaFiz 6-in: (a) a screenshot of the interferometer window in the alignment mode, (b) the fringe pattern, and (c) the measured surface height distribution with about 30-50% undetermined values due to the strong diffraction effect clearly seen in plot (a).

As one can see from Fig. 11c, the measured surface height profile has a large fraction (30-50%) of undetermined height values (seen as black pixels). With the interferometer adjusted to a lower resolution (~130 µm), it is practically impossible to obtain any useful surface height data when measuring the CB sample. We attribute this to a strong diffraction effect caused by the periodicity of the CB pattern, which can be clearly seen during sample alignment (Fig. 11a).

In order to overcome the periodicity-related diffraction problem illustrated in Fig. 11a, we have turned to the use for GD calibration of Fizeau interferometers the targets designed as uniformly redundant arrays. This is because the inherent distribution of the URA elements is binary pseudo-random, while having a more ordered character compared with the highly randomized BPRA patterns. Our expectation is that due to the randomness feature, an URA sample should be significantly free of the diffraction problem. This is based on the earlier work on diffractometry measurements with a one-dimensional (1D) BPR grating, when the observed diffraction pattern had almost perfect white noise character, aka a scattering from a rough surface [37]. The later feature (a relatively ordered character) is useful for the GD calibration data processing.

In order to verify the efficiency of the approach, a URA sample was fabricated on a low cost 6-in diameter and 2 mm thick Si wafer. Figure 12 reproduces the result of the measurements of the prototype URA sample with the ALS XROL Zygo™ DynaFiz in the same arrangement as with the CB sample (Fig. 11).

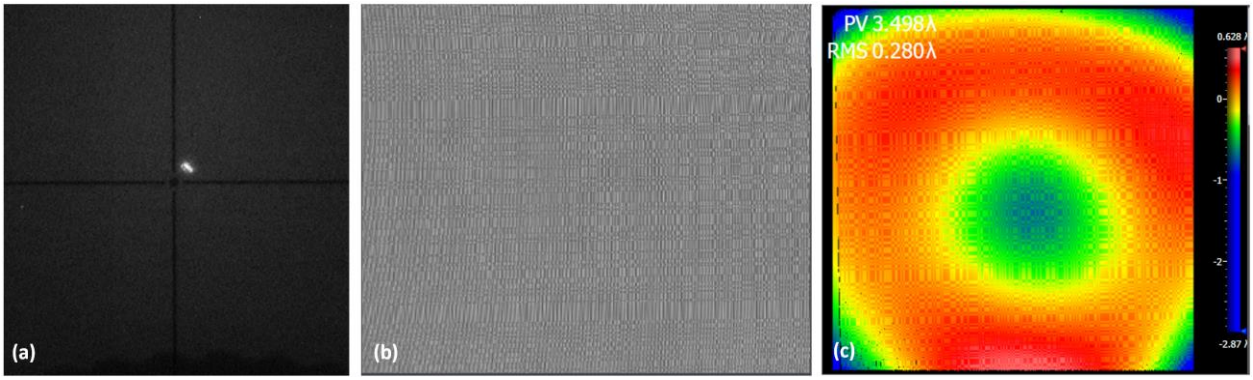

Figure 12: The URA sample with 281 x 283 elements of 360 µm elementary pixel size as measured with the ALS XROL 6-in aperture Fizeau interferometer Zygo™ DynaFiz: (a) a screenshot of the interferometer window in the alignment mode, (b) the fringe pattern shown over almost entire sample area, and (c) the measured surface height distribution after detrending with the best-fit 4yth-order polynomial surface.

In the case of the URA sample, the screenshot of the interferometer window in the alignment mode (Fig. 12a) is free of the regular diffraction effect, showing the desired single spot. The fringe pattern in Fig. 12b, adjusted to the zero-tilt condition, reproduces a perfect URA pattern of the sample. However, the surface height distribution after detrending with the best-fit 4th-order polynomial surface still suffers from a strong low spatial frequency variation that is due to the limited quality of the low-cost substrate used for the proof-of-the-concept investigations.

To summarize the proof-of-concept investigations on the selection and testing of a test pattern suitable for the geometrical distortion characterization of a Fizeau interferometer, we can conclude that the sample patterned according to the URA prescription is a very encouraging option. Further investigation with differently designed URA samples and with different modes of operation of the interferometer is presented in the next subsection.

3.2. Software development for geometrical distortion and data analysis of URA BPRA test artifact

As discussed in the previous subsection, distortion aberration calibration is typically done with a checkerboard test sample; however, the periodic features of such a sample disrupt interferometric measurements by creating strong unwanted interference effects. Therefore, we use a nonperiodic URA BPRA sample for calibration. Such a sample requires a custom algorithm for locating the corner features of the profile image and matching them with the ideal corner locations to characterize the distortion aberration.

The calibration algorithm that we have developed has three stages. First, the BPRA design pattern is registered with the measured surface-height profile. Then the corner features of the measured profile are located with subpixel accuracy. Finally, the parameters of a pinhole camera model including radial distortion are varied to find the values that best project the corners of the design pattern onto those of the measured profile.

Figure 13a shows a surface-height profile of a URA BPRA target etched on a 6-in-diameter wafer measured with the ALS XROL Zygo Verifire Fizeau interferometer. The registration stage of the calibration procedure requires that background surface-height variation be eliminated from the profile, so the measurement is detrended using a spline fit (Fig. 13b). This allows the edges in the profile pattern to be highlighted by taking the square of the height (Fig. 13c).

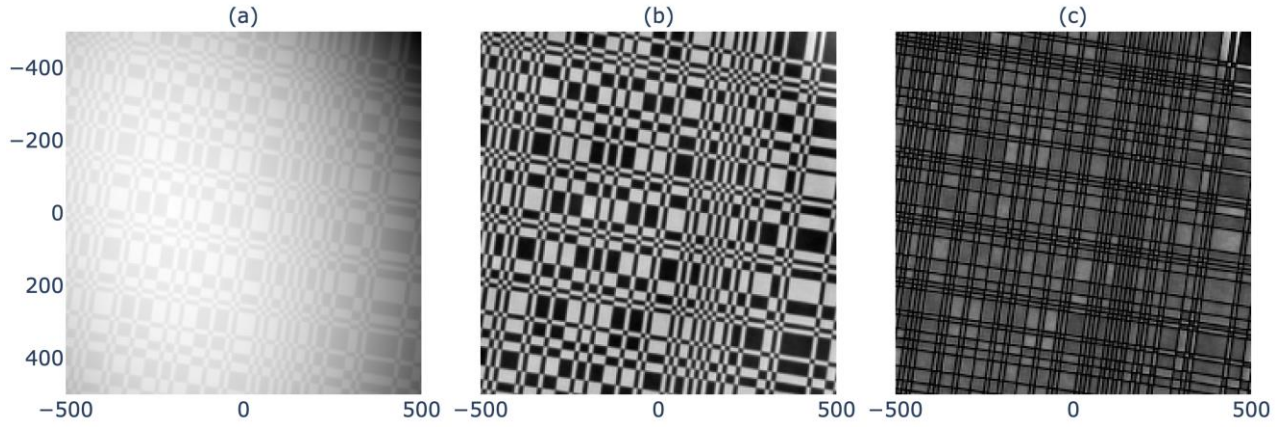

Figure 13: Registration. (a) Surface profile of the URA BPRA target taken with a Zygo Verifire laser interferometer. (b) Profile detrended with a spline fit. (c) Square of the profile, highlighting the grid edges.

The squared-height plot (Fig. 13c) has strong variation along two orthogonal axes. To determine the angle of these axes relative to the image axes, we take the 2D power spectral density (PSD), shown in (Fig. 14). The position of the highest peak in the PSD (shown as an orange dot) relative to the center of the image (the zero-frequency position) provides the approximate rotation angle, here approximately 8 degrees. A more accurate value can be obtained, using the initial angle as a starting point, by integrating over radial paths from the center of the PSD and varying the angle to obtain the maximum integral.

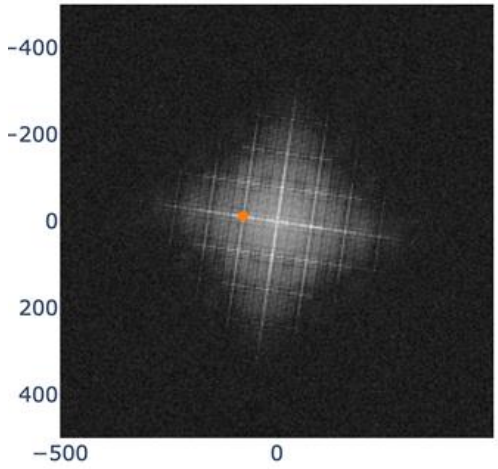

Figure 14: 2D PSD of the squared profile image (in log scale). The orange dot marks the largest peak.

The squared-height plot can now be rotated by the extracted angle to align the grid axes with the image axes. Taking the average over the rows and columns of this image (Fig. 15) provides the grid pattern to be registered with the grid pattern of the target design image.

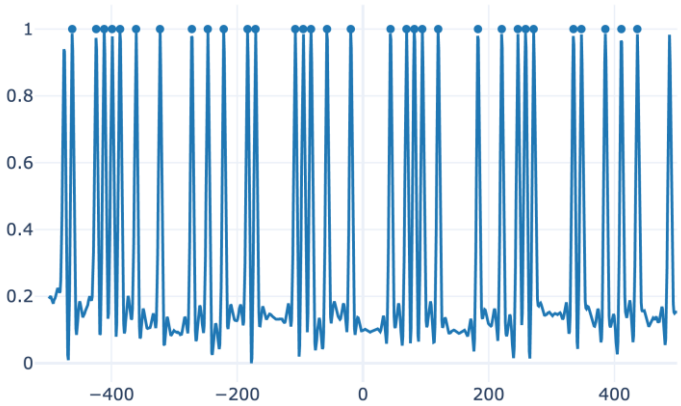

Figure 15: The average of the squared-height profile along one of the grid axes, with the location of the peaks marked by dots.

The minimum distance between adjacent peaks (here approximately 12 pixels) is an estimate of the fundamental feature size of the URA BPRA target as it appears in the interferometer detector image. Using this estimate as a starting point, a fit is performed for each grid axis to find the scale and translation that best matches the measured grid pattern with the design pattern.

The extracted scale and translation vectors are then used to create an initial pinhole camera model used to project the corners of the design pattern onto the image plane (Fig. 16).

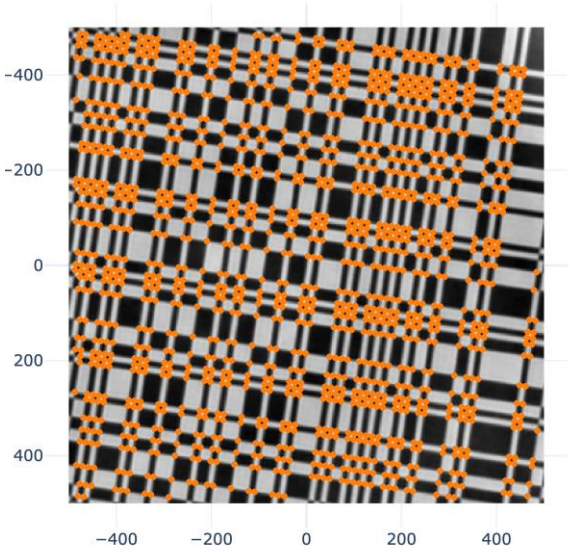

Figure 16: The initial registration of the design image corners, overlaid with the measured profile.

The second stage of the calibration procedure, the refinement of the estimated corner positions to subpixel accuracy, is performed using a "feature map" created from the measured profile that highlights the position of the corners. To create the feature map, first the measured profile is upsampled by a factor of two to reduce aliasing effects in subsequent steps. A section of the upsampled profile is shown in Fig. 17a. Next the upsampled profile is blurred using a rectangular kernel oriented at a 45-degree angle to the grid axes (Fig. 17b). An additional image is created by blurring the profile along the orthogonal direction (Fig. 17c). The squared difference between these two blurred images produces the feature map (Fig. 17d), which has a peak at each corner location in the measured profile.

As the approximate location of each corner is already known from the registration stage of the calibration procedure, accurate subpixel locations can be obtained by fitting a local Gaussian function to the peak that is nearest to each registered corner position.

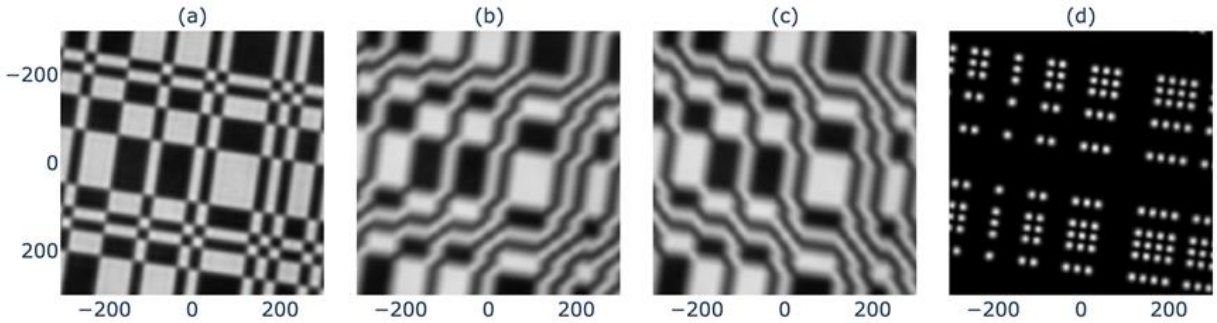

Figure 17: Creating the feature map. (a) A section near the center of the upsampled measured profile. (b) The upsampled profile blurred at 45 degrees to the grid axis. (c) The blur performed in the orthogonal direction. (d) The squared difference between (b) and (c).

In the final stage of the calibration procedure, the measured corner locations, along with the initial estimates of translation, scale, and rotation, are used in a least-squares fit to find the optimal parameters of a full pinhole camera model that projects the corners of the design pattern onto the image plane. The fitted parameters are the two-dimensional translation and three-dimensional rotation of the target, possibly different camera scale factors in the x and y directions, a lowest order radial distortion parameter, and the camera principal point (the center of the radial distortion). The statistical errors for the scale factors (fundamental feature size in the interferometer detector coordinate system) and the z-axis rotation angle are typically very small (a relative error of 10^{-5} in this case). The error in the distortion parameter fit is generally larger (here about 1%).

The magnitude of the fit residuals between the projected design pattern corners and the measured corners are shown in Fig. 18a in units of the detector pixels. The standard deviation of these magnitudes (known as the "reprojection error") is about 0.06 pixel. To illustrate the amount of distortion in the uncalibrated measurement, we can plot the residuals after setting the distortion parameter in the detector model to zero (Fig. 18b). The distortion causes a shift by as much as three pixels at the edges of the measured profile.

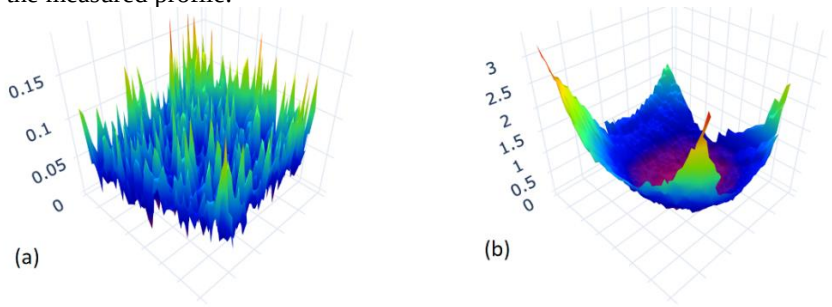

Figure 18: (a) Magnitude of the residuals between the projected design pattern corners and the measured corners in units of detector pixels. (b) Magnitude of the residuals when distortion is neglected in the pinhole camera model, showing the distortion present in the uncalibrated profile.

Based on the algorithm described above, we have developed custom software for geometrical distortion calibration. A graphical user interface for the software has currently been deployed as a web application (Fig. 19).

The process is entirely automatic – the user only needs to choose a surface-height profile measurement for analysis (here we show a Verifire measurement of a 4-in diameter URA target) and specify the prime-number pair that characterizes the URA pattern (here 137×139 elements). The software then registers the URA pattern with the measured image, finds sub-pixel positions of the corner features in the measurement, and finds the best-fit camera model describing the projection from the URA target to the surface-height image.

If there were no distortion in the measurement, the pinhole camera model would describe the projection perfectly, and the fit residuals would be uncorrelated noise. In fact, there is structure in the residuals that describes the geometrical distortion induced by the instrument. This is visualized in the software both as distortion applied to a grid (exaggerated for visibility) and as surfaces describing the x and y residuals (upper plots in Fig. 19). The extracted distortion model can then be used to correct the distortion in a measurement of a SUT (lower plot in Fig. 19).

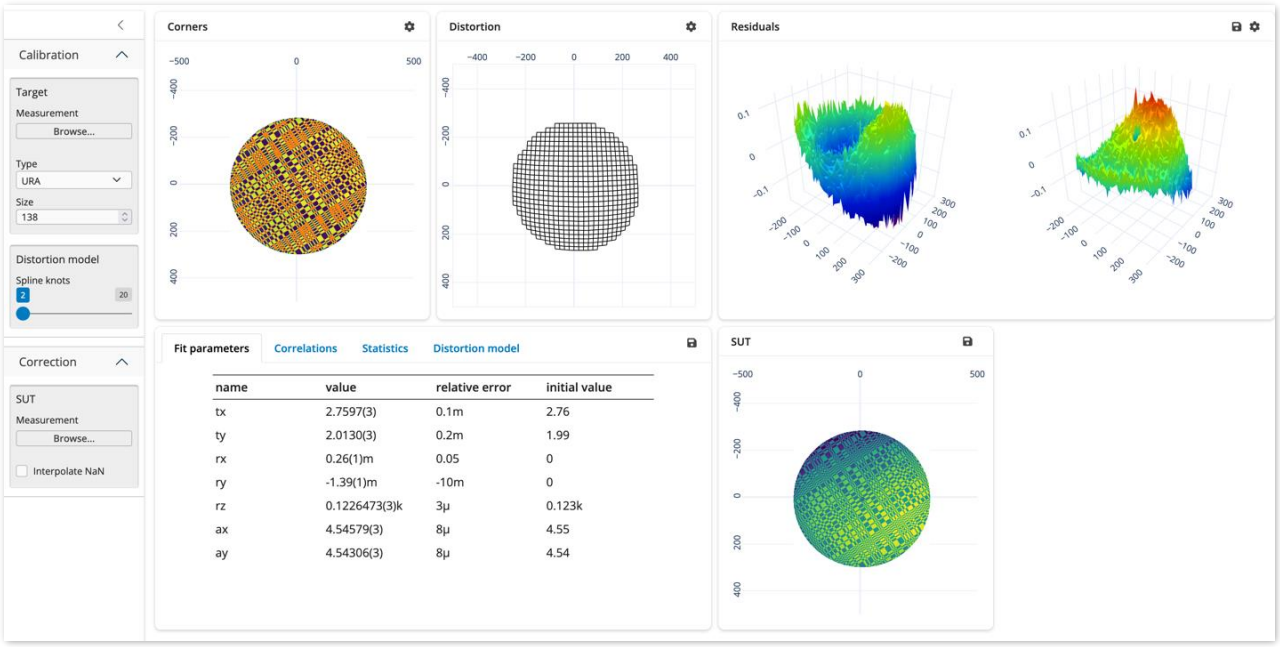

Figure 19: Screenshot of our software for geometrical distortion calibration.

3.3. Geometrical distortion tests of a Fizeau interferometer using 730-μm URA BPRA target

For the geometrical distortion calibration of the ALS XROL 6-in aperture Fizeau interferometer Zigo Verifire™ in the arrangement with the effective pixel size of 160 um (the Zoom setting is 1), we developed a URA BPRA target with the minimum feature size of 730-μm fabricated on a 4-in diameter super-polished substrate.

Figure 20 presents the results of the measurement with the target perfectly aligned (no tilt) and the corresponding data processing using the prototype software described in the previous subsection (Sec. 3.2).

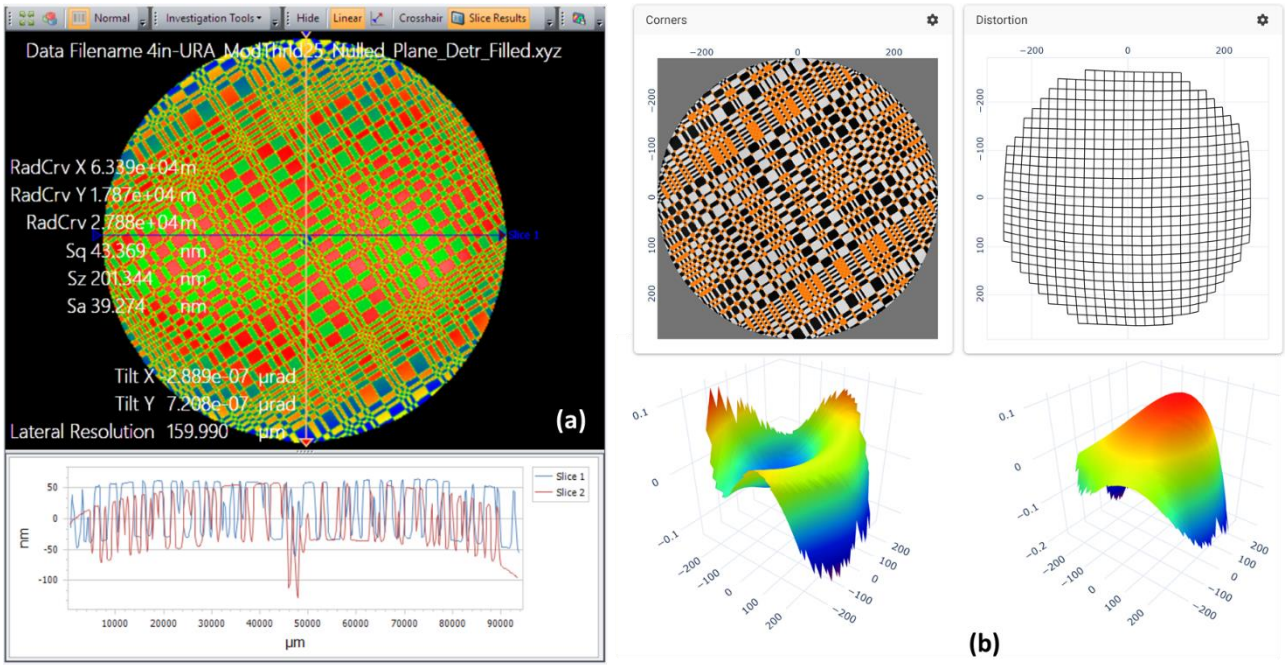

Figure 20: Geometrical distortion calibration of the ALS XROL Zigo Verifire™ Fizeau interferometer using the 730-μm URA BPRA target: (a) the measured target topography and (b) screenshot of the software used to process the data.

Figure 21 shows the GD calibration results similar to Fig. 20, but obtained with the URA target titled in the vertical direction by -502 µrad. In both cases (in Figs. 20a and 21a), the best-fit plane surface detrended. Note that because of the high quality of the substrate, the residual surface figure is significantly better than that of the prototype sample in Fig. 12.

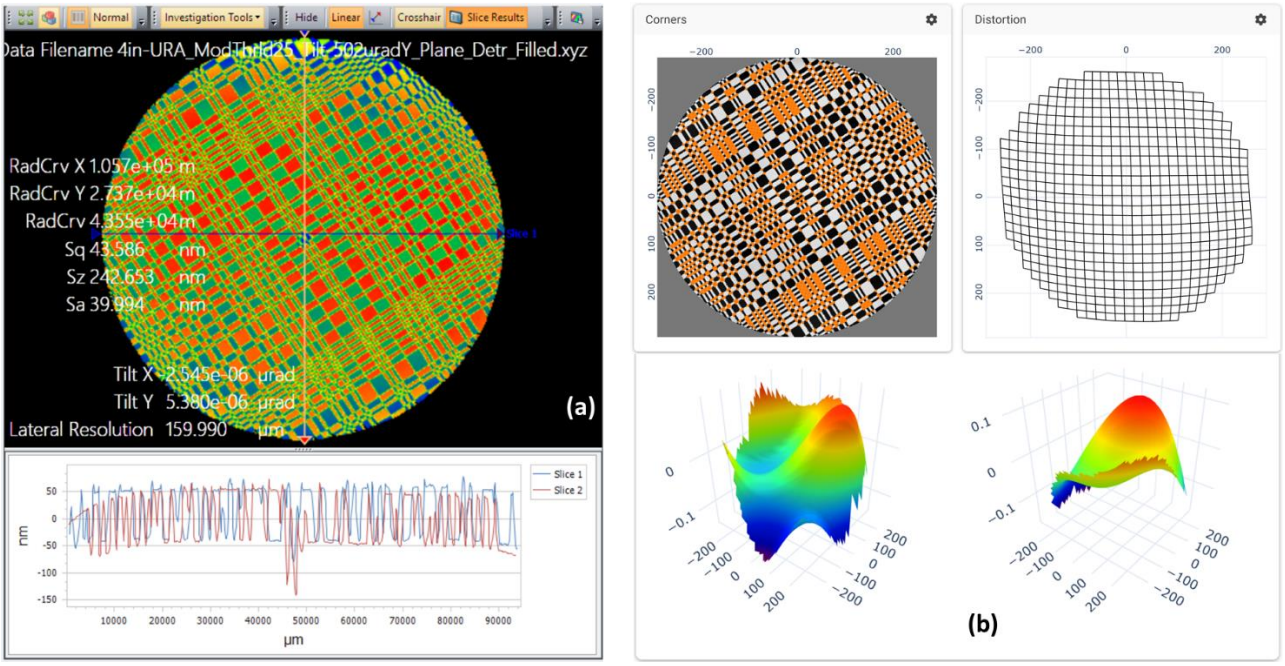

Figure 21: Geometrical distortion calibration of the ALS XROL Zigo Verifire^{TM} Fizeau interferometer using the 730-µm URA BPRA target: (a) the measured target topography and (b) screenshot of the software used to process the data.

The results of the calibration measurements in Figs. 20 and 21 were used to correct the VerifireTM measurements with the plane reference mirror tilted at approximately the same angles. Figure 22 depicts the corrected GD errors.

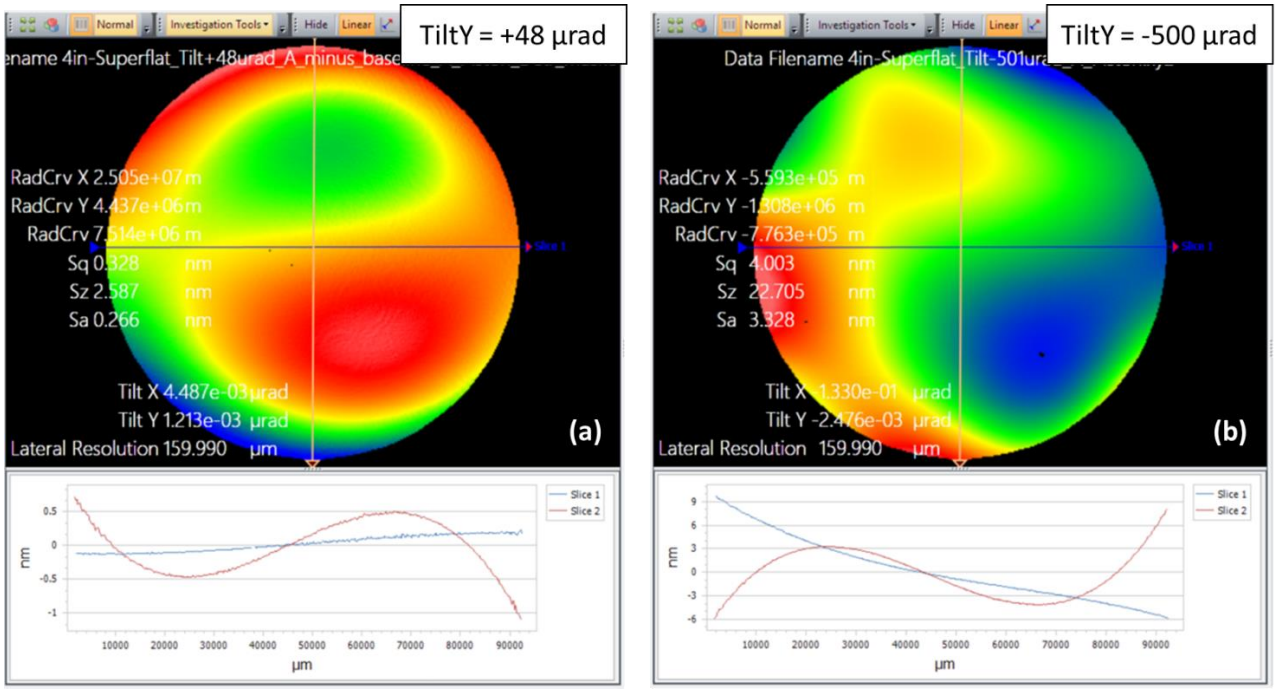

Figure 22: Geometrical distortion errors of the Verifire^{TM} measurements with the plane reference mirror tilted at the vertical tilt angles of (a) +48 µrad and (b) -500 µrad, approximately the same as in the applied calibrations in Figs. 20 and 21.

The corrected geometrical distortion errors shown in Figs. 22a and 22b were calculated as a difference between the measured and corrected surface topographies. The corresponding tilt angles are +48 μrad and (b) -500 μrad. For the correction, we use our prototype software (Sec. 3.2) and the results of the GD calibration in Figs. 20 and 21 performed at approximately the same tilt angles. Unfortunately, because of a relatively simple and low-cost tilting stages used in the current measurement setup (Fig. 2), it is rather difficult to better match the tilt angles of the measurements with the URA target and the plane reference mirror. An improved setup based on a precision hexapod system is under development.

4. CONCLUSIONS

We experimentally investigated critical issues with current stitching Fizeau interferometry (SFI) techniques, including retrace error and geometrical distortion. This is in addition to the investigation of the dependence of the spatial resolution (instrument transfer function) of a Fizeau interferometer performed in the scope of our project on development of high-accuracy SFI [27]. For these investigations, we created a suite of original test artifacts, including the highly randomized (HR) and uniformly redundant array (URA) binary-pseudo random array (BPRA) standards. These artifacts are optimized for comprehensive and precise calibration of Fizeau interferometers.

Using the developed test artifacts, we tested the performance of the ALS XROL Fizeau interferometers. Our experimental data, analyzed with custom data processing and simulation software, revealed a complex interplay of spurious effects, including retrace error (Sec. 2) and geometrical distortion (Sec. 3), and apparent dependence of the power spectral density (PSD) of the surface under test (SUT) on the tilt alignment of the SUT during measurement (see Ref. [27]).

Summarizing the investigation of the real performance of industrial Fizeau interferometers in measurements with tilted and aspherical optics, we can conclude that reliable and accurate SFI will require calibration of the interferometer in the specific experimental arrangement used for SFI measurements and data reconstruction to address the sources of error discussed in this paper and in Ref. [27]. To enable such measurement, we have suggested and are working on development of an adaptive, SUT specific, calibration technique that involves variable-shape calibration artifacts, such as a bent cylinder test system. Our next steps are the integration of the cylindrical bending test system with the ALS XROL Verifire™ Fizeau interferometer and experimental investigations of the SUT curvature dependence of the retrace error, geometrical distortion, and PSD distortion.

ACKNOWLEDGEMENTS

This work was partially supported by the U. S. Department of Energy under contract number DE-AC02-05CH11231 and by the NASA SBIR program under award number 80NSSC22PB039. Research at the Advanced Light Source and the Molecular Foundry at Lawrence Berkeley National Laboratory are supported by the Office of Science, Office of Basic Energy Sciences, and Material Science Division of the U.S. Department of Energy under Contract No. DE-AC02-05CH11231.

DISCLAIMER

REFERENCES

[1] S. Yuan, M. Church, V. V. Yashchuk, K. A. Goldberg, R. Celestre, W. R. McKinney, J. Kirschman, G. Morrison, T. Null, T. Warwick, H. A. Padmore, Elliptically Bent X-ray Mirrors with Active Temperature Stabilization, X-Ray Optics and Instrumentation 2010, 784732/1-9 (2010); doi: 10.1155/2010/784732.

[2] W. R. McKinney, S. C. Irick, J. L. Kirschman, A. A. MacDowell, A. Warwick, V. V. Yashchuk, New Procedure for the Adjustment of Elliptically Bent Mirrors with the Long Trace profiler, Proc. SPIE 6704, 67040G (2007); doi: 10.1117/12.736860.
[3] V. V. Yashchuk, I. Lacey, G. S. Gevorkyan, W. R. McKinney, B. V. Smith, T. Warwick, "Ex situ metrology and data analysis for optimization of beamline performance of aspherical pre-shaped x-ray mirrors at the Advanced Light Source," Rev. Sci. Instrum. 90(2), 021711/1-13 (2019); doi: 10.1063/1.5057441.
[4] V. V. Yashchuk, I. Lacey, and M. Sanchez del Rio, "Analytical expressions of the surface shape of 'diaboloid' mirrors," Proc. SPIE 11493, 114930N/1-13 (2020); doi: 10.1117/12.2568332.
[5] V. V. Yashchuk, K. A. Goldberg, I. Lacey, W. R. McKinney, M. Sanchez del Rio, and H. A. Padmore, "Diaboloidal mirrors: Algebraic solution and surface shape approximations," J. Synchrotron Rad. 28(4), 1031-1040 (2021); http://doi.org/10.1107/S1600577521004860.
[6] M. Sanchez del Rio, K. A. Goldberg, V. V. Yashchuk, I. Lacey, and H. A. Padmore, "Simulations of applications using diaboloid mirrors," J. Synchrotron Rad. 28(4), 1041-1049 (2021); https://doi.org/10.1107/S160057752100401X.
[7] M. Kanaoka, C. Liu, K. Nomura, M. Ando, H. Takino, Y. Fukuda, H. Mimura, K. Yamauchi, and Y. Mori, "Figuring and smoothing capabilities of elastic emission machining for low-thermal-expansion glass optics," J. Vac. Sci. Technol. B. 25, 2110–2113 (2007); https://doi.org/10.1116/1.2789440.
[8] S. Yokomae, H. Motoyama, and H. Mimura, "Development of figure correction system for inner surface of ellipsoidal mirrors, " Precis. Eng. 53, 248–251 (2018); doi: 10.1016/j.precisioneng.2018.04.010.
[9] M. Yabashi, K. Tono, H. Mimura, S. Matsuyama, K. Yamauchi, T. Tanaka, H. Tanaka, K. Tamasaku, H. Ohashi, S. Goto, and T, Ishikawa, "Optics for coherent X-ray applications," J. Synchrotron Rad. 21, 976–985 (2014); doi: 10.1107/S1600577514016415.
[10] Yashchuk, V. V., Lacey, I., Arnold, T., Paetzelt, H., Rochester, S., Siewert, F., and Takacs, P., "Investigation on lateral resolution of surface slope profilers," SPIE Proc. 11109, 111090M/1-19 (2019); doi: 10.1117/12.2539527.
[11] H. Mimura, H. Yumoto, S. Matsuyama, K. Yamamura, Y. Sano, K. Ueno, K. Endo, Y. Mori, M. Yabashi, K. Tamasaku, Y. Nishino, T. Ishikawa, K, Yamauchi, "Relative angle determinable stitching interferometry for hard x-ray reflective optics," Rev. Sci. Instrum. 76, 045102 (2005); https://doi.org/10.1063/1.1868472.
[12] P. de Groot, J. Kramer, T. Sutherland, "Modeling the topographic lateral resolution of interferometers," Proc. of SPIE Vol. 12619, 126190N (2023); doi: 10.1117/12.2670939.
[13] C. Hu, L. Chen, D. Zheng, Y.Wang, Z. Ma, and Z. Zhang, "Iterative correction method of a retrace error in interferometry," Optics Express 30, 37619-37636 (2022); https://doi.org/10.1364/OE.469341.
[14] C. Kreischer, "Retrace error: interferometry's dark little secret," Proc. of SPIE 8884, 88840X (2013); doi: 10.1117/12.2029324.
[15] Morrow, K., da Siva, M. B., Alcock, S., "Correcting retrace and system imaging errors to achieve nanometer accuracy in full aperture, single-shot Fizeau interferometry," Opt. Express 31(17), 27654 (2023); https://doi.org/10.1364/OE.498043.
[16] K. Munechika, K. Yamada, S. Rochester, H. Barnard, W. Chao, I. Lacey, C. Pina-Hernandez, P. Z. Takacs, and V. V. Yashchuk, "Binary pseudo-random array standards for calibration of 3D optical surface profilers used for metrology with significantly curved x-ray optics," the SPIE Optics and Photonics 2024, Conference OP500: Advances in X-Ray/EUV Optics and Components XIX, Symposium: OP24O SPIE Optical Engineering + Applications, Paper 13150-14, (18 - 22 August 2024, San Diego, California, United States); this conference.
[17] K. Munechika, S. Rochester, W. Chao, I. Lacey, C. Pina-Hernandez, D. Padmore, K. Yamada, V. V. Yashchuk, P. Z. Takacs, M. P. Biskach, A. Numata, "Binary Pseudo-random Array (BPRA) for Inspection and Calibration for Cylindrical Wavefront Interferometry," the SPIE Optics and Photonics 2024, Conference OP323: Interferometry and Structured Light 2024, Symposium: OP24O SPIE Optical Engineering + Applications, Paper 13135-4, (18 - 22 August 2024, San Diego, California, United States); this conference.
[18] Boreman, G. D., [Modulation Transfer Function in Optical and Electro-optical Systems], SPIE Press, Bellingham, Washington (2001).
[19] Foreman, M. R., Giusca, C. L., Coupland, J. M., Torok, P., Leach, R. K., "Determination of the transfer function for optical surface topography measuring instruments - a review," Meas. Sci. Technol. 24, 052001/1-18 (2013); doi:10.1088/0957-0233/24/5/052001.
[20] de Groot, P. J., "The instrument transfer function for optical measurements of surface topography," J. Phys. Photonics 3, 024004/1-16 (2021); doi: https://doi.org/10.1088/2515-7647/abe3da.

[21] Yashchuk, V. V., McKinney, W. R., and Takacs, P. Z., "Test surfaces useful for calibration of surface profilometers," United States Patent No.: 8,616,044.
[22] Yashchuk, V. V., Anderson, E. H., Barber, S. K., Bouet, N., Cambie, R., Conley, R., McKinney, W. R., Takacs, P. Z., Voronov, D. L., "Calibration of the modulation transfer function of surface profilometers with binary pseudo-random test standards: expanding the application range to Fizeau interferometers and electron microscopes," Opt. Eng. 50(9), 093604 (2011); doi: 10.1117/1.3622485.
[23] V. V. Yashchuk, S. Babin, S. Cabrini, W. Chao, U. Griesmann, I. Lacey, S. Marchesini, K. Munechika, C. Pina-Hernandez, and A. Roginsky, "Binary pseudorandom array test standard optimized for characterization of large field-of-view optical interferometers," Proc. SPIE 11490, 114900W/1-8 (2020); doi: 10.1117/12.2568309.
[24] Yashchuk, V. V., Artemiev, N. A., Lacey, I., McKinney, W. R., and Padmore, H. A., "Advanced environmental control as a key component in the development of ultra-high accuracy ex situ metrology for x-ray optics," Opt. Eng. 54(10), 104104 (2015); doi: 10.1117/1.OE.54.10.104104
[25] Yashchuk, V. V., Babin, S., Cabrini, S., Griesmann, U., Lacey, I., Munechika, K., Pina-Hernandez, C., and Wang, Q., "Characterization and operation optimization of large field-of-view optical interferometers using binary pseudorandom array test standard," Proc. SPIE 10749, 107490R/1-13 (2018); doi: 10.1117/12.2322011.
[26] V. V. Yashchuk, N. A. Artemiev, I. Lacey, W. R. McKinney, and H. A. Padmore, "Advanced environmental control as a key component in the development of ultra-high accuracy ex situ metrology for x-ray optics," Opt. Eng. 54(10), 104104/1-14 (2015); doi: 10.1117/1.OE.54.10.104104.
[27] V. V. Yashchuk, K. Munechika, S. Rochester, P. Z. Takacs, I. Lacey, and K. Yamada, "Performance of Plane Wavefront Fizeau Interferometers in Power Spectral Density Measurements with Tilted Plane Optics," the SPIE Optics and Photonics 2024, Conference OP500: Advances in X-Ray/EUV Optics and Components XIX, Symposium: OP24O SPIE Optical Engineering + Applications, SPIE SPIE Proc. Paper 13150-11 (2024); this conference.
[28] K. Kinnstaetter, A. W. Lohmann, J. Schwider, and N. Streibl, "Accuracy of phase shifting interferometer," Appl. Opt. 27, 5082-5089 (1988); https://doi.org/10.1364/AO.27.005082.
[29] C. Huang, "Propagation errors in precision Fizeau interferometry," 32(34), 7016-7021 (1993); https://doi.org/10.1364/AO.32.007016.
[30] L. Deck and C. Evans, "High performance Fizeau and scanning white-light interferometers for mid-spatial frequency optical testing of free-form optics," Proc. SPIE 5921, 59210A (2005); doi: 10.1117/12.616874.
[31] I. Lacey, K. Anderson, G. P. Centers, R. D. Geckeler G. S. Gevorkyan, A. Just, T. Nicolot, B. V. Smith, and V. V. Yashchuk, "The ALS OSMS – Optical Surface Measuring System for high accuracy two-dimensional slope metrology with state-of-the-art x-ray mirrors," Proc. SPIE 10760, 1076002/1-20 (2018); doi: 10.1117/12.2321347.
[32] R. Su, Y. Wang, J. Coupland, and R. Leach, "On tilt and curvature dependent errors and the calibration of coherence scanning interferometry," Opt. Exp. 25(4) 3297-3310 (2017); https://doi.org/10.1364/OE.25.003297.
[33] AMETEK/Zygo Corporation, "DynaFiz® Confident Metrology for a Dynamic World;" https://www.Zygo.com/products/metrology-systems/laser-interferometers/dynafiz.
[34] W.-J. Peng, C.-F. Ho, W.-L. Lin et al., "Design and tolerance analysis of a transmission sphere by interferometer model," Proc. SPIE 9582, 958208 (2015); 10.1117/12.2187759.
[35] K. Munechika, S. Rochester, W. Chao, I. Lacey, C. Pina-Hernandez, and V. V. Yashchuk, "Binary pseudo-random array standards for calibration of 3D optical surface profilers used for metrology with aspheric x-ray optics," SPIE Proc. 12223, 1222307/1-19 (2022); doi: 10.1117/12.2633163.
[36] S. Rochester, D. English, I. Lacey, K. Munechika, and V. V. Yashchuk, "Towards super-resolution interference microscopy metrology of x-ray variable-line-spacing diffraction gratings: Recent Developments," SPIE Proc. 12240, 122400E/1-14 (2022); doi: 10.1117/12.2633637.
[37] S. K. Barber, E. D. Anderson, R. Cambie, W. R. McKinney, P. Z. Takacs, J. C. Stover, D. L. Voronov, V. V. Yashchuk, "Binary Pseudo-Random Gratings and Arrays for Calibration of Modulation Transfer Function of Surface Profilometers," Nucl. Instr. and Meth. A 616, 172-182 (2010); https://doi.org/10.1016/j.nima.2009.11.046.
[38] R. Petre, D. A. Content, J. P. Lehan, S. L. O'Dell, S. M. Owens, W. A. Podgorski, J. Stewart, and W. W. Zhang, "The Constellation-X Spectroscopy X-ray Telescope," Proc. SPIE 5488, 505-514 (2004); doi: 10.1117/12.552062.
[39] M. Guainazzi, R. Willingale, L. W. Brenneman, E. Bulbul, J.-W. A. den Herder, E. Kuulkers, J.-U. Ness, and L. Natalucci, "On the scientific impact of the uncertainties in the Athena mirror effective area ," J. Astron. Telesc. Instrum. Syst. 8(4), 044002 (2022); https://doi.org/10.1117/1.JATIS.8.4.044002.